Letters in Applied NanoBioScience
Open-Access Journal (ISSN: 2284-6808)

Article
Volume 13, Issue 1, 2024, 21
https://doi.org/10.33263/LIANBS131.021

Utilization of Eastern Nigerian Propolis Extract for Synthesis of Corrosion Inhibitive Silver Nanoparticles on Carbon Steel in Acidic Medium

Godwin Abawulo Ijuo [1,*], Pius Oziri Ukoha [2], John Ogbaji Igoli [3]

[1] Department of Chemistry, Federal University of Agriculture, PMB, 2373, Makurdi, Nigeria; ijuo.godwin@uam.edu.ng (G.A.I.);
[2] Department of Pure and Industrial Chemistry, University of Nigeria, Nsukka; pius.ukoha@unn.edu.ng (P.O.U.);
[3] Department of Chemistry, Federal University of Agriculture, PMB, 2373, Makurdi, Nigeria; j.o.igoli@uam.edu.ng (J.O.I.);
* Correspondence: ijuo.godwin@uam.edu.ng (G.A.I.);

Scopus Author ID (Nil)

Received 26.10.2022; Accepted: 7.01.2023; Published: 13.08.2023

Abstract: The high cost of production and potentially harmful effects of inorganic corrosion inhibitors on the ecosystem necessitated the search for a low-cost, efficient, and environmentally friendly alternative. Due to their high surface-to-volume ratio and capacity to create self-assembled films on metal surfaces, benign nanoparticles present a good alternative. In this study, Eastern Nigerian propolis extracts were utilized to synthesize silver nanoparticles and were characterized spectroscopically. The composites were then tested for corrosion-inhibitive potentials in HCl solution. The characteristic surface plasmon resonance (SPR) absorption bands were obtained at around 420 nm. The XRD results showed that the resultant crystalline silver nanoparticles of Eastern Nigerian Propolis Extract (ENPE-AgNPs) has FCC structure, with a mean nanoparticle size of 5.067 ± 1.465. The STEM image revealed several oval structures that were densely filled with AgNPs, which appeared as white spots, with patterns that appeared homogeneous. In the presence of 1000 ppm ENPE-AgNPs, the results showed high inhibition efficiency of 98.23 and 91.34 % for EIS and gravimetric technique, respectively. Also, the thermodynamic and adsorption characteristics of ENPE-AgNPs on CS in HCl solution were calculated. It was discovered that the ENPE-AgNPs performed well as an inhibitor of CS corrosion in HCl.

Keywords: propolis; nanoparticles; carbon steel; corrosion inhibition; adsorption.

1. Introduction

Metals frequently dissolve more quickly when they come into contact with a hostile environment. This irreversible degradation drastically reduces the useful life of metallic materials, affecting home and industrial properties [1,2]. The World Corrosion Organization's most recent survey estimates that the global direct cost of corrosion is between €1.3 and €1.4 trillion, or 3.1 to 3.5% of a country's GDP, excluding the harm that corrosion causes to the environment, the waste of resources, the loss in production, or personal injury [3].

Carbon steel is the most widely used metal in the industry, making up about 85% of the steel produced each year [4,5]. This suggests carbon steel is significantly involved in corrosion, making it one of the most sensitive metals. Due to their efficiency, affordability, and environmental friendliness, organic compounds are now the preferred replacement for synthetic inhibitors, which have been banned due to their toxicity to humans and the

environment [6]. Heteroatoms such as nitrogen, oxygen, sulfur, and phosphorus present in the compounds make it easier for such compounds to bind to metal surfaces and form protective films that block the active sites, reducing the metal's contact with environmental elements [7,8].

Propolis has comparatively high flavonoid content. These flavonoids have features that can be used as corrosion inhibitors, such as conjugated double bonds, electronegative atoms, and aromatic rings [9]. Honeybees prepare the resinous glue known as propolis from flowers and leaf buds to serve as a crack sealer, wall smoother, temperature and moisture content regulator, as well as preserve the hive environment aseptic throughout the year. The season in which propolis is gathered, the time it was formed, the plants from which the ingredients are obtained, the location of the hive, and the types of bees used all play a role in propolis' color and composition [10,11]. Most propolis has been discovered to contain a blend of waxes, pollen, essential and aromatic oils, and other organic materials, including bee enzymes. Since it possesses a wide range of biological features and uses in medicine, propolis has attracted the interest of researchers.

With a few adjustments, corrosion inhibition research can make use of remarkable capacity of nanomaterials to build self-assembling coatings on metal surfaces. Silver nanoparticles are particularly recognized to have greater reactivity toward acidic aqueous solutions [12–13]. Recent studies have shown that composites made of organic molecules and nanoparticles are excellent at preventing carbon steel from corrosion under acidic conditions [14–16].

2. Materials and Methods

To create 6.00 cm^2 surface area coupons, 0.12 cm thick carbon steel (CS) was cut into 3 x 2 cm coupons. The coupon samples underwent polishing, ethanol degreasing, acetone drying, and storage in a desiccator. The corrosive media for the experiment was a 1.0 M solution of hydrochloric acid Reagents of analytical grade were utilized in this experiment. Before usage, the solvents n-hexane, ethyl acetate, and methanol underwent one more distillation. Water that had been twice distilled was used to prepare all the reagents.

2.1. Preparation and extraction of propolis samples.

Samples of propolis were obtained from a bee farmer in Enugu, Eastern Nigeria (Figure 1). The propolis samples were mashed with a pestle and mortar after being air-dried for two weeks. The 100 g of finely ground materials were first macerated for 72 hours at room temperature to remove fat using n-hexane. The marc was re-extracted using ethyl acetate and methanol after filtration with Whatman No. 1 filter paper using a vacuum pump. A rotating vacuum evaporator was used to extract the solvents from the mixture entirely. Until used, the powdered extracts were then stored in opaque vials at 4 °C.

2.2. Synthesis of propolis silver nanoparticles (ENPE-AgNPs).

The method used to synthesize ENPE-AgNPs was identical to that described in [17]. Reducing silver nitrate solution in the presence of the propolis extract constituted the basis for producing ENPE-AgNPs composite. 100 mL of de-ionized water was added to a beaker holding 1.0 g of propolis extract with vigorous shaking for 1 hour. 100 mL of 1.0 mM $AgNO_3$ was then added, and the mixture was stirred at 25 °C for 48 hours. Visual observation of color

change was by UV/Vis spectrophotometer. The pellets were collected and stored after centrifuging to separate the produced silver nanoparticles. The supernatant was discarded.

Figure 1. Propolis samples.

2.3. Characterization of ENPE-AgNPs.

The spectroscopic evaluation was used to keep track of the bioreduction of silver ions. Using a JENWAY 6405 UV-visible spectrophotometer with a resolution of 0.1 nm, bandwidth of 5 nm, and a scan speed of 1000 nm/min, absorption measurements in the 190-1100 nm range were performed. X-ray Diffractometer Thermo Scientific model: ARL'XTRA goniometer system, with h, k, and l values, was used to conduct the X-ray diffraction (XRD) examination. SEM (Phenom Pro, 800-07334, Netherlands) operating at 15 kV was used to examine the surface morphology of ENPE-AgNPs. GeminiSem-500-70-18 Scanning Transmission Electron Microscopy was used to conduct additional research on the image and the diffraction pattern (STEM). Fourier Transfer-Infra Red (FT-IR) spectroscopy (Agilent Cary 630 FTIR fitted with ZnSe optics and a DTGS detector) was used to examine the functional groups on the sample.

2.4. Corrosion inhibition test.

2.4.1. Gravimetric measurement.

Pre-weighed CS coupons were submerged in 200 mL of 1.0 M HCl. The ENPE-AgNP concentrations utilized in this study ranged from 200, 400, 600, 800, and 1000 ppm. Tests were run for 24, 48, 72, 96, 120, 144, and 168 hours at room temperature. For three hours of immersion duration, the effect of temperature was also tested at 303, 313, 323, and 333 K, respectively. The CS coupons were taken out of the acid-inhibitor system once the immersion period had passed, cleaned, dried, and weighed. The weight loss was taken to be the difference between the coupon's initial and final weight at a particular period. Every test was carried out in duplicate. The inhibition efficiency (%IE) and corrosion rate of mild steel were calculated from the weight loss results, according to equations 1 and 2 [18],

$$IE_{\exp} = \left(1 - \frac{W_{(1)}}{W_{(0)}}\right) x100 \quad (1)$$

where, $W_{(0)}$ is the weight loss of the mild steel without inhibitor and $W_{(1)}$ is the weight loss of mild steel with inhibitor.

$$CR\left(gh^{-1}cm^{-2}\right) = \frac{\Delta W}{At} \quad (2)$$

where ΔW is the weight loss, A is the coupon area, and t is the immersion time.

2.4.2. Electrochemical impedance spectroscopy (EIS).

The experiments were conducted at 303 K using 200 mL of test solution. A conventional three-electrode system consisting of CS as a working electrode, an auxiliary electrode, and a reference electrode was used for the measurements. The %IE were calculated from the charge transfer resistance (R_{ct}) values by using the equation

$$\%IE = \frac{R_{ct} - R_{ct}^0}{R_{ct}} \times 100 \quad (3)$$

where, R_{ct}^0 is the charge transfer resistance of MS without inhibitor, and R_{ct} is the charge transfer resistance of CS with an inhibitor. The double layer capacitance (C_{dl}) was calculated using Equation 4

$$C_{dl} = \frac{1}{2\pi f_{max} R_{ct}} \quad (4)$$

where f_{max} is the frequency at which the imaginary component of impedance is maximum.

3. Results and Discussion

3.1. Synthesis and characterization.

The reduction of Ag^+ was confirmed by the change in color of the reaction mixture from milky to yellowish brown (Figure 2). The apparent color change has been attributed to the excitation of Surface Plasmon vibration in silver nanoparticles [19].

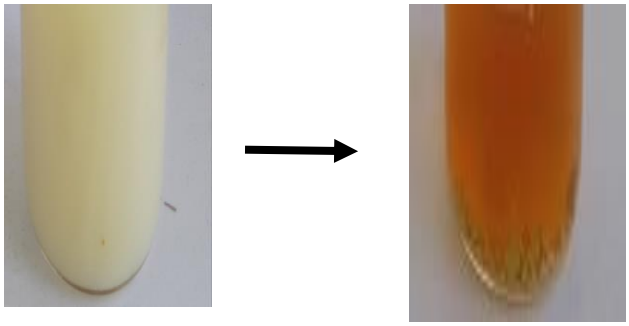

Figure 2. Optical color change of raw propolis extracts in de-ionized water and the final silver dispersion formed after reduction of 1 mM $AgNO_3$ solution with ENPE.

The synthesized ENPE-AgNPs' UV-vis absorption spectra (Figure 3) revealed that the Surface Plasmon Resonance band occurred between 414 and 422 nm, forming a peak at roughly 420 nm [20]. According to studies, UV/Vis light with a wavelength of 420 nm is absorbed by tiny particles with diameters between 5 and 10 nm [21]. The ENPE-AgNPs have modest diameters, less than 20 nm, as indicated by the maximum at 420 nm.

The ENPE-AgNPs' X-ray diffractogram (Figure 4) reveals three Ag-related diffraction peaks at 2 = 38.25, 44.68, and 65.74. The (111), (200), and (220) planes are represented by these three primary peaks, respectively. The face-centered cubic structure (fcc) of AgNPs from ENPE, which is the basis for the Bragg reflection crystallographic planes, supported the crystallinity of the Ag nanoparticles.

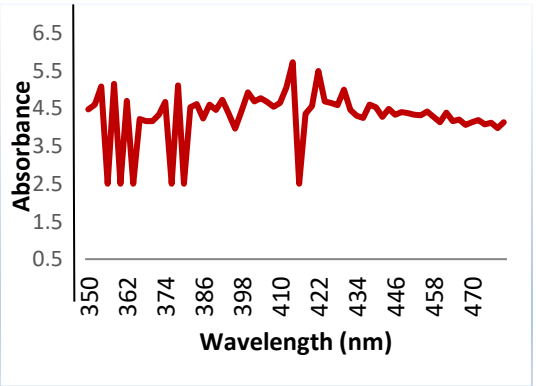

Figure 3. UV-vis absorption spectra of ENPE-AgNPs.

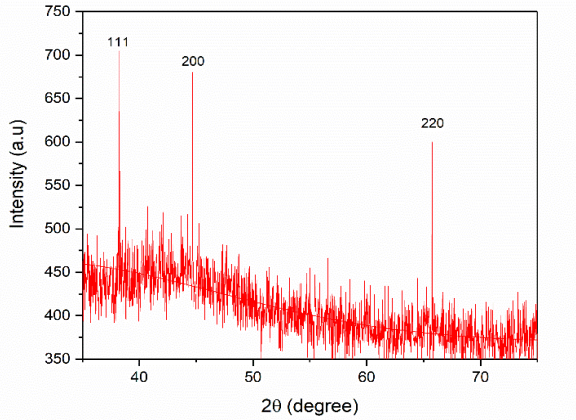

Figure 4. X-ray Diffraction Spectrum of ENPE-AgNPs.

Scherer's equation (5) was used to determine the average crystallite size, which was discovered to be 4.44 nm [22,23].

$$D = \frac{K\lambda}{\beta Cos\theta} \qquad (5)$$

More information on the morphology and size characteristics of the silver nanoparticles is revealed by SEM/EDX. Examination of the SEM/EDX image (Figure 5) reveals a homogeneous distribution of ENPE-AgPs. It was discovered that all nanoparticles had a spherical shape, which is in good accord with the shape of the Surface Plasmon Resonance (SPR) band in UV-Vis spectra. Due to silver's dominance, the findings of the EDX study revealed a significant absorption peak of silver at 3 keV. The existence of a substrate on which the NP sample was supported during SEM imaging likely caused the emergence of additional elements. As can be observed from the grain size distribution histogram of silver nanoparticles in Figure 6, further processing of the SEM results resulted in a mean particle size of 5.06782 ± 1.46578. This is in agreement with previous data and XRD results [24,25].

The invention of Scanning Transmission Electron Microscopy nanodiffraction, STEM, allows for the simultaneous acquisition of the image and the diffraction pattern of single nanostructures [26,27]. Different nano-objects investigated in vacuum have been subject to STEM nanodiffraction, including ferritins [28], nanotubes [29], nanoalloys [30], nanoparticles [31], and hard alloys [32]. Due to its quick and potentially automated acquisition approach for nanodiffractions, this method has advantages.

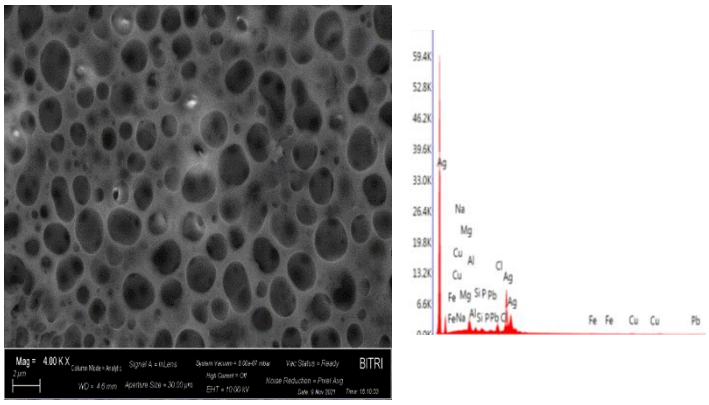

Figure 5. Scanning Electron Microscopy/Energy Dispersive (SEM/EDX) of ENPE-AgNPs.

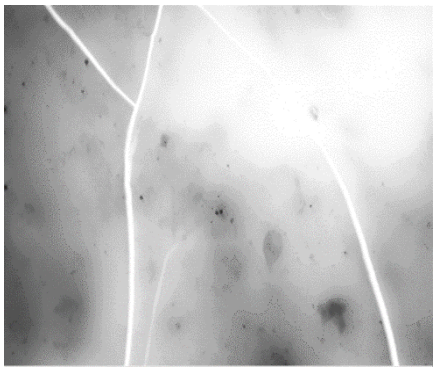

Figure 6. Scanning Transmission Electron Microscopy (STEM) Spectra of ENPE-AgNPs.

Another benefit of the method is the potential for comprehensive structural investigation of nanomaterials with a considerably better information limit than direct imaging. This is due to the fact that in reciprocal space, the level of structural complexity is only constrained by the observable range of electron scattering.

STEM nanodiffraction enables identifying the individual structure of significantly more randomly oriented nano-objects in an assembly in real-world applications. Size and shape impacts on the structural characteristics of nanostructures were revealed by such statistically significant structural investigations [33].

The STEM image (Figure 6) showed several oblong or circular structures that were densely filled with AgNPs, which are visible as black spots and have a homogeneous pattern. The level of Ag-NP overlap in these picture regions was sufficiently low to distinguish between and possibly count individual NPs, resulting in a uniform distribution of the AgNPs across the studied areas. This distribution suggests that the NPs are localized [34].

3.2. Corrosion inhibition test.

3.2.1. Weight loss measurements.

Table 1 presents the inhibition efficiencies of the inhibitor on mild steel in 1.0 M HCl calculated from equation 1. The results show that as the inhibitor's concentration was raised, the effectiveness of the inhibition increased. Figure 7 displays the corrosion rates in the absence and presence of the inhibitors using Equation 2. It was discovered that the corrosion rate increased with time but decreased with a rise in inhibitor concentration. This behavior may be explained by the fact that if the inhibitor's concentration increases, more of it will bind to the metal or the solution's surface [35]. The increased surface-to-volume ratio of the nanoparticles due to their sizes is linked to the high inhibitory efficiency [36]. Additionally, Ituen *et al*., 2021 have linked improved adsorption capability and the existence of larger electron clouds around heteroatoms such as O, N, S, and other atoms to higher inhibitory efficiency of nanoparticles than raw extracts [37]. The corrosion rates discovered by investigation in the absence and presence of the inhibitors, as shown in Figure 8, increased over time but decreased with an increase in inhibitor concentration.

At 303, 313, 323, 333, and 343 K, in the absence and presence of various concentrations of the inhibitor, it was examined how temperature affected the inhibitor's ability to inhibit the corrosion of CS in 1.0 M HCl. The results are presented in Table 2. The inhibition efficiencies rise with higher inhibitor concentrations but fall with higher temperatures, following a similar pattern to the findings for the influence of time, however, with varying inhibition efficiencies that are weaker with the effect of temperature. Additionally, it was discovered that the corrosion rates rose with temperature, as illustrated in Figure 9. This is proof that ENPE-AgNPs effectively prevent the corrosion of CS in hydrochloric acid. The adsorption type, where the inhibitor is physically adsorbed at lower temperatures but chemisorption is preferred at higher temperatures, has also been implicated in decreased inhibitory efficacy with rising temperatures [38]. Here, physisorption was preferred.

Table 1. Inhibition efficiencies of ENPE-AgNPs on CS in 1.0 M HCl.

Time (hrs)	Inhibitor Concentration (ppm)					
	Blank	**200**	**400**	**600**	**800**	**1000**
24	-	71.27	74.81	74.90	76.05	76.73
48	-	71.49	74.61	76.12	77.28	80.51
72	-	72.22	74.30	75.03	77.73	78.92

Time (hrs)	Inhibitor Concentration (ppm)					
	Blank	200	400	600	800	1000
96	-	81.33	82.19	84.00	84.28	86.95
120	-	87.00	87.19	90.35	90.44	95.21
144	-	88.03	89.21	89.62	90.48	96.09
168	-	91.30	93.54	95.48	96.65	98.23

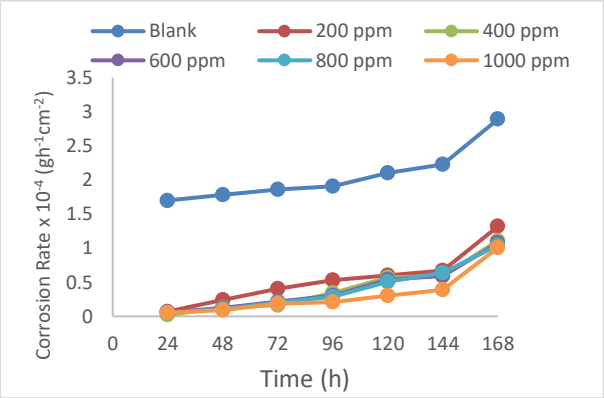

Figure 7. Corrosion rates of CS in 1.0 M HCl in the absence and presence of the various concentration of ENPE-AgNPs as a function of immersion time (h).

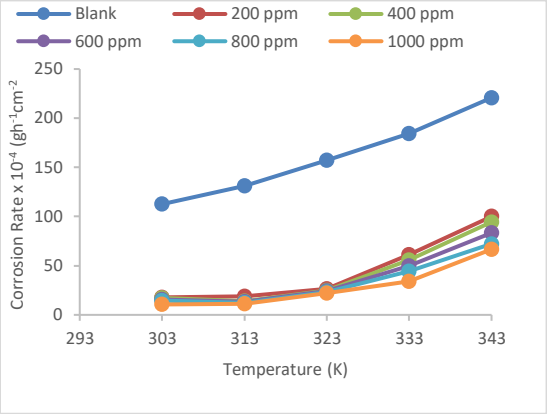

Figure 8. Corrosion rates of CS in 1.0 M HCl in the absence and presence of the various concentration of ENPE-AgNPs as a function of temperature (K).

Table 2. Inhibition Efficiencies of the Inhibitors on CS in 1.0 M HCl at 303 – 343 K.

Temperature (K)	Inhibitor Concentration (ppm)					
	Blank	200	400	600	800	1000
303	-	62.37	65.76	78.46	82.54	94.93
313	-	60.02	60.66	63.93	67.21	68.85
323	-	57.21	58.48	61.13	63.54	66.81
333	-	56.42	57.65	57.89	60.12	65.06
343	-	48.45	53.15	51.58	55.34	59.43

3.2.2. Electrochemical measurements.

Electrochemical Impedance Spectroscopy (EIS) measurements at open-circuit potential were carried out to determine the kinetic parameters for electron transfer reactions at the steel/electrolyte interface and simultaneously regarding the surface properties of the investigated system. A suitable equivalent circuit was used to analyze the impedance data, depending on the shapes of the Nyquist plots. A simplest Randles equivalent circuit (Figure 9) was used to fit the Nyquist plot in the absence and presence of the inhibitor in a 1.0 M hydrochloric acid solution. It consists of a fast charge transfer process R1, the surface layer resistance R2, and one constant phase element (CPE). By adding R1 and R2 at various inhibitor doses, the polarization resistance Rp, which is comparable to charge transfer resistance Rct, was obtained. The % inhibition efficiency from equation 3 was then calculated using the resulting Rct. Additionally, using equation 4, the double layer capacitance (Cdl) was computed. The charge transfer resistance (Rct), constant phase element (CPE), and inhibitory efficiencies are the parameters acquired from the measurement of EIS, as indicated in Table 3.

The carbon steel electrode's Nyquist plots in 1.0 M HCl solution in both the absence and presence of various inhibitor concentrations are shown in Figure 10. According to the Nyquist plot, raising the inhibitor concentration results in a rise in both the diameter of the semicircles. One single depressed semicircle shape was produced using the impedance diagram. This suggests that charge transfer mostly regulates the corrosion process [39]. Without the inhibitors, the modulus of the Nyquist plots in 1.0 M HCl solution was significantly lower than it was with the inhibitors. The diameter of the semicircles and the values of Rct

increased as the inhibitor concentration increased, as shown by the Nyquist plots. This effect can be attributed to the increased concentration of absorbed inhibitor molecules on the surface of the mild steel.

Additionally, this suggests an improvement in corrosion inhibition effectiveness (Table 3). According to the ohmic rule, which states that V = iR, the more resistance (Rct), the less electrical current I flows, and the fewer electrons that pass the metal surface. Mild steel's cathodic oxidation is so prevented. The semicircles' identical shapes in both the absence and presence of the inhibitors point to a similar corrosion mechanism regardless of the inhibitors' presence. As a result, adding inhibitors has little effect on how the CS corrodes in 1.0 M HCl solution. The surface heterogeneity is the reason why the value of "n" is less than 1, according to [40,41].

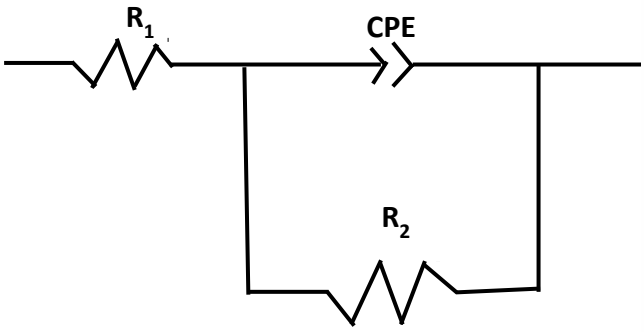

Figure 9. Equivalent circuits used to fit experimental EIS data for the corrosion of the CS in 1.0 M hydrochloric acid solution in the absence and presence of the inhibitor.

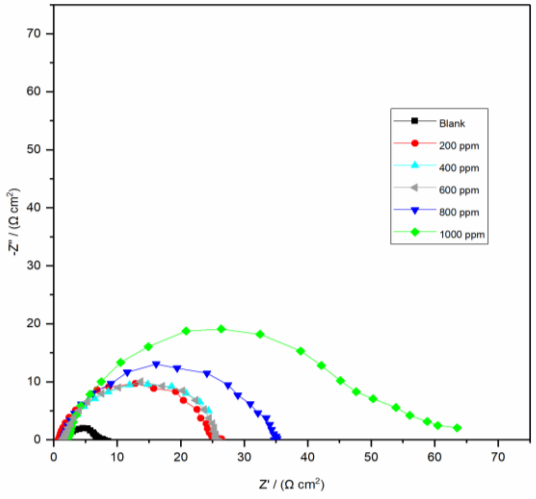

Figure 10. Nyquist plots for the CS specimen in 1.0 M HCl in the absence and presence of different concentrations of ENPE-AgNPs.

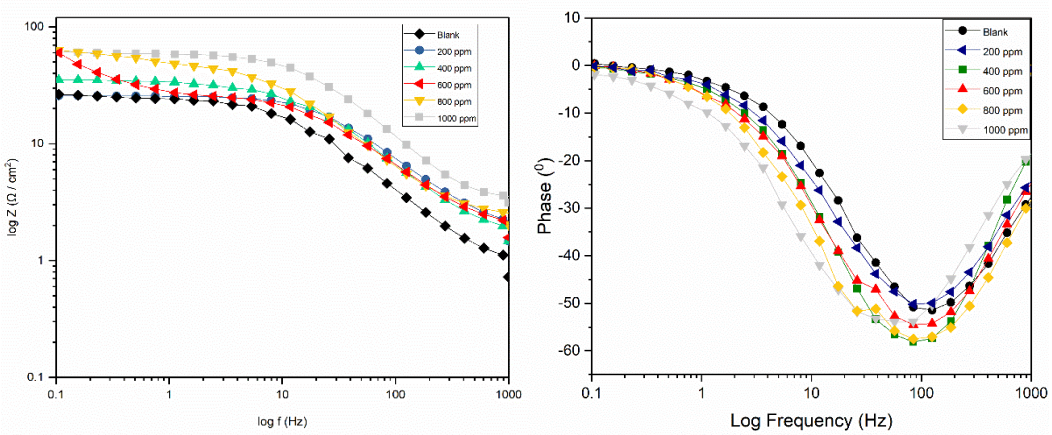

Figure 11. (a). Bode impedance ; **(b).** Bode phase plots for CS electrode in the absence presence of ENPE-AgNPs in 1.0 M HCl.

The Nyquist diagrams are not perfect semicircles, a phenomenon that is referred to as the frequency dispersion of interfacial impedance. This is due to the surface roughness or inhomogeneity of the metal surface associated with solid metal electrodes because of the presence of a non-ideal frequency response for which constant phase element CPE was used [42].

The Bode impedance and Bode phase charts for the CS electrode in the presence and absence of ENPE-AgNPs in 1.0 M HCl solution are shown in Figure 11, respectively. It is clear that the Bode plot only contains a single capacitive loop. An increase in the inhibitor concentration led to larger negative phase angle values at the intermediate frequency, as shown from the Bode phase plot. Phase angle readings became more negative as the concentration of the different inhibitors rose. This suggests that the inhibitive behavior happened due to more inhibitor molecules being adsorbed at the surface of mild steel [43].

Table 3. Impedance parameters for the corrosion of CS in 1.0 M HCl in the absence and presence of various concentrations of the inhibitors.

Concentration (ppm)	R_1 (Ω cm^2)	R_2 (Ω cm^2)	R_{ct} (Ω cm^2)	C_{dl} (μF cm^{-2})	n	%IE
Blank	1.205	10.414	11.619	9.34 x 10^{-4}	0.88	-
200	12.243	22.400	34.643	2.62 x 10^{-4}	0.97	66.46
400	17.534	44.349	61.883	1.18 x 10^{-4}	0.86	81.22
600	22.546	57.979	80.525	6.76 x 10^{-5}	0.88	85.57
800	41.653	72.124	113.777	6.68 x 10^{-5}	0.89	89.79
1000	52.144	82.095	134.239	2.21 x 10^{-6}	0.91	91.34

3.2.3. Thermodynamic consideration.

In order to understand the mechanism by which ENPE-AgNPs inhibit the corrosion of CS in 1.0 M HCl, the thermodynamic behavior of the inhibitors was carefully examined. The transition state plots were used to determine thermodynamic parameters such as the energy of activation (EA), standard enthalpy (H), and the entropy changes of adsorption (S). The corrosion rate is related to these thermodynamic factors by the transition state equation (equation 6), which was further reduced to a linear formula (7).

$$CR = \frac{RT}{Nh}\exp\left(\frac{\Delta S_{ads}}{R}\right)\exp\left(\frac{-\Delta H_{ads}}{RT}\right) \quad (6)$$

$$\log\left(\frac{CR}{T}\right) = \log\left(\frac{R}{Nh}\right) + \left(\frac{\Delta S_{ads}}{2.303R}\right) - \left(\frac{\Delta H_{ads}}{2.303RT}\right) \quad (7)$$

The Arrhenius curve for the corrosion of CS in 1.0 M HCl with varying inhibitor concentrations is shown in Figure 12A. The calculated parameters are listed in Table 4. The Table shows that the values for the activation energy are larger when the inhibitor is present than when it is absent. With an increase in inhibitor concentration, the Ea values likewise went up.

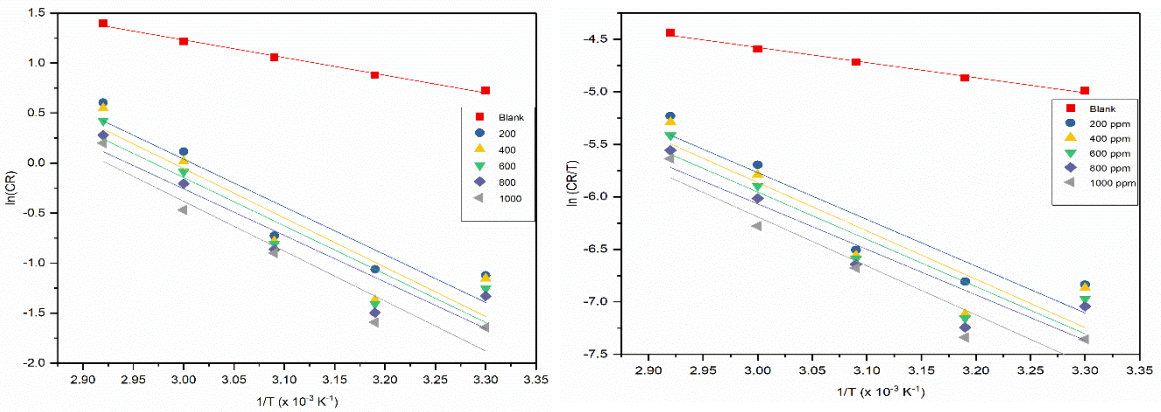

Figure 12. (**a**) Arrhenius and (**b**) Transition State plot for the corrosion of CS in 1.0 M HCl containing the various concentration of ENPE-AgNPs.

In the absence of ENPE-AgNPs, the lowest value of Ea (14.68 KJmol^{-1}) was found. Ea values grew steadily with increasing inhibitor concentrations, reaching their highest values of 41.71 KJmol^{-1} in the presence of 1000 ppm of the inhibitor. Because of the energy barrier and mass transfer provided by the adsorbed ENPE-AgNPs, the corrosion rate has decreased [44]. According to reports, a value of Ea larger than 80 KJ mol^{-1} indicates chemical adsorption as opposed to physical adsorption, which occurs when Ea is less than 80 KJ mol^{-1} [45]. The fact that all of the Ea values obtained through experimentation are less than 80 KJmol^{-1} indicates that the additives were physically adsorbed onto the coupons. Therefore, it may be said that the multilayer protective coverage on the entire surface of the CS was achieved.

Table 4. Transition state and Arrhenius parameters for the corrosion of CS in 1.0 M HCl containing various inhibitor concentrations.

Concentration (ppm)	ΔS^0_{ads} (J/mol)	ΔH^0_{ads} (J/mol)	Ea (J/mol)	R^2
Blank	-199.68	-11.97	14.68	0.99
200	-134.47	-37.02	39.72	0.90
400	-131.48	-38.27	40.12	0.84
600	-134.81	-38.41	40.89	0.87
800	-139.97	-38.59	41.47	0.87
1000	-132.74	-38.76	41.71	0.93

The enthalpy and entropy of adsorption of the inhibitor are related to the corrosion rate of a metal by equation 8;

$$CR = \frac{RT}{Nh}\exp^{\left(\frac{\Delta S_{ads}}{R}\right)}\exp^{\left(\frac{-\Delta H_{ads}}{RT}\right)} \quad (8)$$

with CR representing the corrosion rate of the CS, while R and N stand for gas constant Avogadro's number, respectively, Planck's constant and temperature are denoted with h and T, respectively. The entropy adsorption of the inhibitor on a metal is ΔS_{ads} and ΔH_{ads} is the enthalpy of adsorption of the inhibitor on the CS [46]. Equation (8) can be transformed into a linear form by taking the logarithm of both sides of the equation to obtain equation (9),

$$\log\left(\frac{CR}{T}\right) = \log\left(\frac{R}{Nh}\right) + \left(\frac{\Delta S_{ads}}{2.303R}\right) - \left(\frac{\Delta H_{ads}}{2.303RT}\right) \quad (9)$$

From equation (9), a straight line graph of log (CR/T) versus 1/T was obtained (Figure 12), giving $\Delta H_{ads}/2.303R$ and (log(R/Nh) + $\Delta S_{ads}/2.303R$), as the slope and intercept, respectively. Figure 12B shows the transition state plots for the corrosion of CS in 1.0 M HCl in the absence and in the presence of the various concentration of the inhibitor. The corresponding transition state parameters obtained from the plots are recorded in Table 4. The exothermic nature of the CS dissolution in 1.0 M HCl is confirmed by the negative values of the enthalpy of activation for the inhibitor established. The values of ΔH_{ads} are less than 100 kJ/mol, supporting the physisorption nature of the CS dissolution in 1.0 M HCl. The values of ΔS are negative and decreased progressively with an increase in the inhibitor concentration, indicating that the inhibitor molecules freely moving in the bulk solution were adsorbed orderly onto the carbon steel surface. This implies that the activation complex represents association steps and that the reaction was spontaneous and feasible [47].

3.2.4. Adsorption consideration.

The Langmuir isotherm plots of log C/θ against log C for the adsorption of ENPE-AgNPs at various temperatures are shown in Figure 13. The equilibrium constant of adsorption

of the inhibitors on the CS surface is related to the standard free energy of adsorption ΔG^0_{ads} by equation 10.

$$\Delta G^0 ads = -2.303RT \log (55.5Kads) \quad (10)$$

where R is the molar gas constant, T is the absolute temperature, and 55.5 is the water concentration in solution expressed in mol L^{-1}. Langmuir parameters for the corrosion of mild steel in 1.0 HCl containing various concentrations of the inhibitor calculated from the slope and intercept of the plots are presented in Table 5.

The effectiveness of organic compounds as corrosion inhibitors can be ascribed to the molecules' adsorption through their polar functions on the metal surface. Adsorption isotherm values are important to explain the corrosion inhibition mechanism of organo-electrochemical reactions of metals and alloys. Equation 23 shows the general form of adsorption isotherms. Different adsorption isotherms were tested in order to obtain more information about the interaction between the mild steel surface and at various temperatures. The linear regression coefficients (R^2) were used to determine the best fit. Langmuir adsorption isotherm was found to be the best fit, in which case the linear regression coefficients (R^2) were close to unity. Langmuir adsorption isotherm assumes that the solid surface contains a fixed number of adsorption sites, and each site holds one adsorbed species [48].

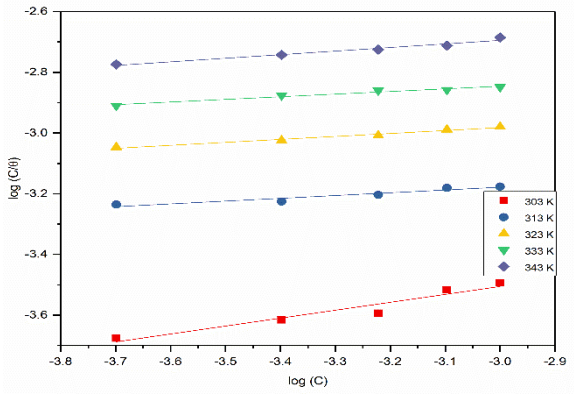

Figure 13. Langmuir isotherm for the adsorption of ENPE-AgNPs on CS surface in 1.0 M HCl solution at various temperatures.

Table 5. Langmuir parameters for the corrosion of CS in 1.0 HCl containing various concentrations of the studied inhibitor.

T (K)	Slope	Intercept	R^2	k_{ads}	ΔG^0_{ads} (kJ/mol)
303	0.2607	-2.7233	0.9362	0.0019	-5.68
313	0.0915	-2.9039	0.9192	0.0012	-6.95
323	0.0975	-2.6895	0.9788	0.0020	-5.85
333	0.0869	-2.5851	0.9652	0.0026	-5.36
343	0.1181	-2.3403	0.9633	0.0046	-3.91

3.2.5. FTIR study.

Table 6 lists the frequencies and peaks that can be inferred from the ENPE-AgNPs' spectra (Figure 14). The outcome demonstrates the formation of two novel alcohol-induced IR adsorption bands. In the corrosion product, O-H stretching at 3383 cm^{-1} changed to 3275 cm^{-1} with weaker intensity. This change indicates how the ENPE-AgNPs and carbon steel interact [49]. Since they are absent from the spectrum of the corrosion products, other IR absorption bands in the frequency range of 2922-833 cm^{-1} in the spectrum of ENPE-AgNPs were used for

adsorption on the surface of the carbon steel. C-H stretching, C=O stretching, N-O stretching, C=C stretching, C-O stretching, and C-N stretching are among the affected functional groups.

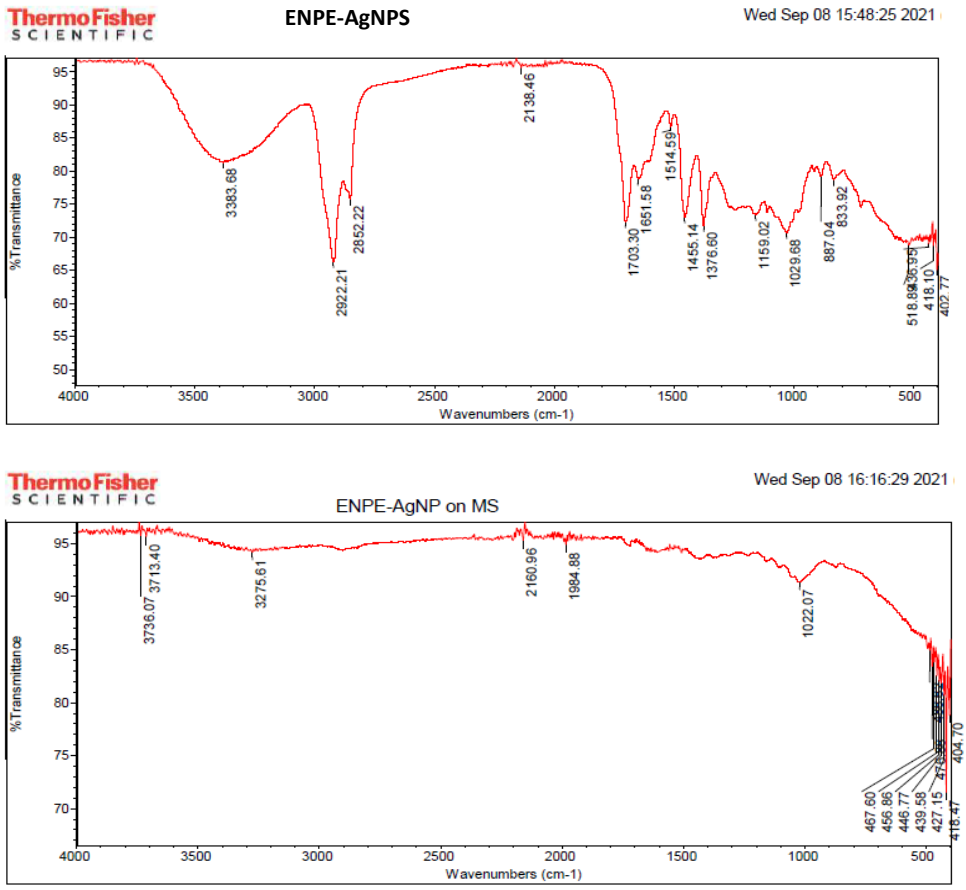

Figure 14. FTIR spectrum of **(A)** ENPE-AgNPs and **(B)** Corrosion product when ENPE-AgNPs was the inhibitor for the corrosion inhibition of mild steel in 1.0 M HCl.

Table 6. Frequencies and peak intensities of FTIR absorption by ENPE-AgNPs and the corrosion product of the CS in the presence of ENPE-AgNPs.

ENPE before adsorption		Corrosion product in the presence of ENPE		Functional group/assignment
Frequency (cm^{-1})	Intensity	Frequency (cm^{-1})	Intensity	
		3736.07	weak	alcohol
		3713.40	weak	alcohol
3383.68	Broad, strong	3275.61	weak	O-H stretching
2922.21	Strong, sharp			O-H stretching
2852.22	strong			C-H stretching
1703.30	strong			C=O stretching
1651.58	medium			C=C stretching
1514.59	medium			N-O stretching
1455.14	strong			O-H Alcohol
1376.60	strong			O-H bending
1159.02	medium			C-O stretching tertiary alcohol
1029.68	strong	1022.07	medium	C-N stretching
887.04	strong			C-H bending
833.92	strong			C-H stretching

4. Conclusion

Synthesis and characterization of ENPE-AgNPs were effectively carried out. The mean particle size of the synthesized nanoparticles was found to be 5.06782 ± 1.46578. Treatment of the face-centered cubic structured (fcc) crystalline ENPE-AgNPs by Scherer's equation gave

the average crystallite size of 4.44 nm. ENPE-AgNPs have proven to be a good inhibitor for the corrosion of carbon steel in HCl. The %IE using gravimetric and electrochemical impedance spectroscopy methods was found to increase to a maximum of 98.23 and 91.34, respectively, in the presence of 1000 ppm. The effectiveness of this inhibitor was, however, lowered by the rise in temperature. The negative values of entropy change of adsorption (ΔS) imply that the inhibitor molecules freely moving in the bulk solution were adsorbed orderly onto the carbon steel surface. Also, the activation complex represents association steps, and the reaction was spontaneous and feasible. Also, results showed that all the enthalpy of activation (ΔH) for the inhibitors are negative, reflecting the exothermic nature of the CS dissolution process in HCl. The physically adsorbed ENPE on the mild steel surface in HCl was found to obey Langmuir adsorption isotherm. The results of this study reveal that the ENPE-AgNPs are a low-cost, green, and effective inhibitor of the corrosion of CS.

Funding

This research received no external funding.

Acknowledgments

This research has no acknowledgments.

Conflict of Interests

The authors declare no conflict of interest.

References

1. Umoren, P.S.; Kavaz, D.; Umoren, S.A. Corrosion Inhibition Evaluation of Chitosan–CuO Nanocomposite for Carbon Steel in 5% HCl Solution and Effect of KI Addition. *Sustainability* **2022**, *14*, 7981, https://doi.org/10.3390/su14137981.
2. Orokpo, A. M. ; Wuana, R. A.; Chuhul, H.F.; Eneji, I.S. Corrosion Inhibition Potential of Benue Propolis Extracts on Carbon Steel in 1.0 M Hydrochloric Acid Medium: Experimental and Computational Studies. *PCBR*. **2022**, *5*, 283-300, https://doi.org/10.22034/pcbr.2022.354920.1231.
3. George, F.; Hays, P.E. International Symposium on Corrosion for Sustainable development, World Corrosion Organization, Hilton Phuket Arcadia, Thailand. **2022**. https://www.scientific.net/AMR.95.-2.pdf
4. Popoola, L. T.; Yusuff, A. S.; Ikumapayi, O. M.; Chima, O. M.; Ogunyemi, A. T.; Obende, B. A. Electrochemical, Isotherm, and Material Strength Studies of Cucumeropsis mannii Shell Extract on A515 Grade 70 Carbon Steel in NaCl Solution. *Hindawi Int. J of Corrosion* **2022**, *2022*, 3189844, https://doi.org/10.1155/2022/3189844.
5. Fazal B. R.; Becker T.; Kinsella B.; Lepkova K. A review of plant extracts as green corrosion inhibitors for CO_2 corrosion of carbon steel. *npj Mater Degrad.* **2022**, *6*, 5, https://doi.org/10.1038/s41529-021-00201-5.
6. Fouda1, A. S.; El-Desoky, H. S.; Abdel-Galeil, M. A.; Mansour, D. Niclosamide and dichlorphenamide: new and effective corrosion inhibitors for carbon steel in 1M HCl solution. *SN App Sci*. **2021**, *3*, 287, https://doi.org/10.1007/s42452-021-04155-w.
7. Aralu, C. C.; Chukwuemeka-Okorie, H. O.; Akpomie, K. G. Inhibition and adsorption potentials of mild steel corrosion using methanol extract of *Gongronema latifoliuim*, *App. Water Sci*. **2021**, *11*, 22, https://doi.org/10.1007/s13201-020-01351-8.
8. Jennifer K. B.; Claudia H.; David S.; Kevin H.; Agnes P.; Gustavo F. Honey Bees on the Move: From Pollination to Honey Production and Back. Economic Research Service, ERR-290, USDA. *Economic Research Service*. **2021**, 1-27, Washington, DC, https://www.nass.usda.gov/Education_and_Outreach/Reports,_Presentations_and_Conferences/reports/ERS-290-09-12-2022.pdf.
9. Wagh, V.D. Propolis, a wonder bees product and its pharmacological potentials. *Adv Pharmacol Sci* **2013**, 308249, https://doi.org/10.1155/2013/308249.

10. Burdock, G.A. Review of the biological properties and toxicity of bee propolis. *Food and Chem Tox.* **1998**, *36*, 347–363, http://dx.doi.org/10.1016/S0278-6915(97)00145-2.
11. Patil, S.; Desai, N.; Mahadik, K.; Paradkar, A. Can green synthesized propolis loaded silver nanoparticulate gel enhance wound healing caused by burns?. *Euro J of Int. Med.* **2015**, S1876-3820, 00043-8, https://doi.org/10.1016/j.eujim.2015.03.002.
12. Nayak, D.; Ashe, S.; Rauta, P.R. Bark extract mediated green synthesis of silver nanoparticles: Evaluation of antimicrobial activity and antiproliferative response against osteosarcoma. *Mater Sci Eng*, **2016**, *58*, 44–52, https://doi.org/10.1016/j.msec.2015.08.022.
13. Ayman, M.A.; Hamad, A. A.; El-Mahdy, G. A.; Abdel-Rahman, O. E. Application of Stabilized Silver Nanoparticles as Thin Films as Corrosion Inhibitors for Carbon Steel Alloy in 1M Hydrochloric Acid. Hindawi Publishing Corp. *J nanomaterials* **2013**, https://doi.org/10.1155/2013/580607.
14. Quadri, T.W., L.O. Olasunkanmi, O.E. Fayemi, Zinc oxide nanocomposites of selected polymers: synthesis, characterization, and corrosion inhibition studies on mild steel in HCl solution. *ACS Omega* **2017**, *2*, 8421–8437, https://doi.org/10.1021/acsomega.7b01385.
15. Solomon, M.M.; Gerengi H.; Umoren S.A. Gum Arabic – silver nanoparticles composite as a green anticorrosive formulation for steel corrosion in a strong acid media. *Carbohyd Polym* **2018**, *181*, 43–55, https://doi.org/10.1016/j.carbpol.2017.10.051.
16. Asafa, T.B.; Durowoju, M.O.; Madingwaneng, K.P.; Diouf, S.; Sadiku, E.R.; Shongwe, M.B.; Olubami, P.A.; Ismail, O.S.; Ajala, M.T.; Oladosun, K.O. Gr-Al composite reinforced with Si_3N_4 and SiC particles for enhanced microhardness and reduced thermal expansion. *Appl. Sci.* **2020**, 1026, https://doi.org/10.1007/s42452-020-2838-5.
17. Ijuo, G. A.; Nguamo, S.; Igoli, J. O. Ag-nanoparticles Mediated by *Lonchocarpus laxiflorus Stem Bark* Extract as Anticorrosion Additive for Mild Steel in 1.0 M HCl Solution. *PCBR*. **2022**, *5*, 133-146, https://doi.org/10.22034/pcbr.2022.324366.1208.
18. Odewole, O.A.; Ibeji, C.U.; Oluwasola, H.O.; Oyeneyin O.E.; Akpomie K.G.; Ugwu C.M.; Ugwu C.G.; Bakare T.E. Synthesis and anti-corrosive potential of Schiff bases derived 4-nitrocinnamaldehyde for mild steel in HCl medium: experimental and DFT studies. *J Mol Struct*, **2021**, *1223*, 129214, https://doi.org/10.1016/j.molstruc.2020.129214.
19 Meena, H. P.; Singh, A. P.; Tejavath, K. K. Biosynthesis of Silver Nanoparticles Using Cucumis prophetarum Aqueous Leaf Extract and Their Antibacterial and Antiproliferative Activity Against Cancer Cell Lines. *ACS OMEGA*, **2020**, *2020*, 5520−5528, https://doi.org/10.1021/acsomega.0c00155.
20. Shameli, K.; Ahmad, M. B.; Al-Mulla, E.A.J.; Ibrahim, N.A.; Shabanzadeh, P.; Rustaiyan, A.; Abdollahi, Y.; Bagheri, S.; Abdolmohammadi, S.; Usman, M.S.; Zidan, M. Green biosynthesis of silver nanoparticles using Callicarpa maingayi stem. *Molecules* **2016**, *17*, 8506-8517, https://doi.org/10.3390/molecules17078506.
21. Bilal, M.; Rasheed, T.; Iqbal, H.M.; Li, C.; Hu, H.; Zhang, X. Development of silver nanoparticles loaded chitosan-alginate constructs with biomedical potentialities. *Int. J. Biol. Macromol*, **2017**, *105*, 393−400, https://doi.org/10.1016/j.ijbiomac.2017.07.047.
22. Lee, Y.J.; Song, K.; Cha, S.H.; Cho, S.; Kim, Y.S.; Park, Y. "Sesqui terpenoids from Tussilago farfara flower bud extract for the eco-friendly synthesis of silver and gold nanoparticles possessing antibacterial and anticancer activities. *Nanomaterials*." **2019**, *9*, https://doi.org/10.3390/nano9060819.
23. Oyeneyin, O. E.; Ojo, N. D.; Ipinloju, N.; Agbafa, E. B.; Emmanuel, A. V. Investigation of the corrosion inhibition potentials of some 2-(4-(substituted) arylidene)-1H-indene-1,3-dione derivatives: density functional theory and molecular dynamics simulation. Beni-Suef University Journal of Basic and Applied Sciences **2022,** *11*, 132, https://doi.org/10.1186/s43088-022-00313-0.
24. Logeswari, P.; Silambarasan, S.; Abraham, J. Synthesis of silver nanoparticles using plant extract and analysis of their antimicrobial properties. *J Saudi Chem Soc*, **2015**, *19*, 311–317, https://doi.org/10.1016/j.jscs.2012.04.007.
25. Al Banna, L. S.; Salem, N. M.; Jaleel, G. A.; Awwad A. M. Green synthesis of sulfur nanoparticles using Rosmarinus officinalis javanica leaves extract and nematicidal activity against Meloidogyne. *Chem. Intl.* **2020**, *6*, 3, https://doi.org/10.5281/zenodo.3528019.
26. Cowley, J. M. Electron nanodiffraction," micro. research and technique, **1999**, *46*, 75–97,https://doi.org/10.1002/(sici)1097-0029(19990715)46:2<75::aid-jemt2>3.0.co;2-s.
27. Liu, J. Advances and Applications of Atomic-Resolution Scanning Transmission Electron Microscopy. *Microscopy and Microanalysis* **2021**, *27*, 943–995, https://doi.org/10.1017/S1431927621012125.
28. Kalinin, S. V.; Ophus, C., Voyles, P. M.; Erni, R.; Kepaptsoglou, D., Grillo, V.; Lupini, A. R.; Oxley, M. P., Schwenker, E.; Chan, M. K. Y.; Etheridge J.; Li, X.; Han, G. G. D.; Ziatdinov, M.; Shibata, N.; Pennycook, S. J. Machine learning in scanning transmission electron microscopy. *Nature Reviews Methods Primers*, **2022**, *2*, https://doi.org/10.1038/s43586-022-00095-w

29. Cowley, J.M.; Janney, D. E.; Gerkin, R. C; Buseck, P. R. The Structure of Ferritin Cores Determined by Electron Nanodiffraction. *J Str. B*, **2000**, *131*, 210-216, https://doi.org/10.1006/jsbi.2000.4292
30 Cowley, J.M. Off-axis STEM or TEM holography combined with four-dimensional diffraction imaging. *Microsc Microanal*, **2004**, *10*, 9-15, https://doi.org/10.1017/S1431927604040267.
31. Alloyeau, D.; Ricolleau, C.; Oikawa, T.; Langlois, C.; Le Bouar, Y.; Loiseau, A. STEM nanodiffraction technique for structural analysis of CoPt nanoparticles. *Ultramicroscopy*. **2008**, *108*, 7, 656-662, https://doi.org/10.1016/j.ultramic.2007.10.006.
32. Kharlamov, V.O.; Krokhalev, A. V.; Kuz'min, S.V.; Ysak, V.I. Investigation of the Structure and Distribution of Chemical Elements between the Phases of Hard Alloys of the Cr_3C_2-Ti System, Obtained at Various Modes of Explosive Compaction. *Mats. Sci. Forum*, **2020**, *992*, 487-492, https://doi.org/10.4028/www.scientific.net/MSF.992.487.
33. Alloyeau, D.; Ricolleau, C.; Oikawa, T.; Langlois, C.; Le Bouar, Y.; Loiseau, A. Size and shape effects on the order-disorder phase transition in CoPt nanoparticles. *Nat Mater*. **2009**, *12*, 940-946, https://doi.org/10.1038/nmat2574.
34. Peckys, D. B.; de Jonge, N. Visualizing Gold Nanoparticle Uptake in Live Cells with Liquid Scanning Transmission Electron Microscopy. *Nano Lett*. **2011**, *11*, 1733–1738, https://doi.org/10.1021/nl200285r.
35. Ijuo, G. A.; Orokpo, A. M.; Tor, P. N. Effect of *Spondias mombin* Extract on the Corrosion of Mild Steel in Acid Media. *Chem. Res. J*. **2018**, *3*, 64-77, https://chemrj.org/download/vol-3-iss-3-2018/chemrj-2018-03-03-64-77.pdf.
36. Iroha, N. B.; Dueke-Eze, C.U.; Fasina, T. M.; Anadebe, V. C.; Guo, L. Anticorrosion activity of two new pyridine derivatives in protecting X70 pipeline steel in oil well acidizing fuid: experimental and quantum chemical studies. *J Iran Chem Soc.* **2021**, *19*, 1–16, https://doi.org/10.1007/s13738-021-02450-2.
37. Ituen, E.; Yuanhua, L.; Verma, C.; Alfantazi, A.; Akaranta, O.; Ebenso, E. E. Synthesis and characterization of walnut husk extract-silver nanocomposites for removal of heavy metals from petroleum wastewater and its consequences on pipework steel corrosion. *J Mol. Liq.* **2021**, *335*, 116132, https://doi.org/10.1016/j.molliq.2021.116132.
38. Zhou, Z.; Seif, A.; Pourhashem, S.; Silvestrelli, P. L.; Ambrosetti, A.; Mirzaee, M.; Duan, J.; Rashidi, A.; Hou, B. Experimental and Theoretical Studies toward Superior Anti-corrosive Nanocomposite Coatings of Aminosilane Wrapped Layer-by-Layer Graphene Oxide@MXene/Waterborne Epoxy. *ACS App. Mat.s & Interf.* **2022**, *14*, 51275-51290, https://doi.org/10.1021/acsami.2c14145.
39. Akpan, A.; Offiong, N.O. Electrochemical linear polarization studies of Amodiaquine drug as a corrosion inhibitor for mild steel in 0.1M HCl solution. *Chem Mater Res* **2015**, *7*, https://core.ac.uk/download/pdf/234666572.pdf.
40. Nazari, M. H.; Shihab, M. S.; Cao, L.; Havens, E. A.; Shi, X. A peony-leaves-derived liquid corrosion inhibitor: protecting carbon steel from NaCl," Green Chem. *Let. and Rev.* **2017**, *10*, 359–379, https://doi.org/10.1080/17518253.2017.1388446.
41. Songbo, R.; Ying, G.; Chao, K.; Song, G.; Shanhua, X.; Liqiong, Y. Efects of the corrosion pitting parameters on the mechanical properties of corroded steel. *Constr Build Mater*. **2021**, *272*, 121941, https://doi.org/10.1016/j.conbuildmat.2020.121941.
42. Iroha, N. B.; Maduelosi, N. J. Corrosion Inhibitive Action and Adsorption Behaviour of *Justicia Secunda* Leaves Extract as an Eco-Friendly Inhibitor for Aluminium in Acidic Media. *BRIAC* **2021**, *11*, 13019 – 13030, https://doi.org/10.33263/BRIAC115.1301913030.
43. Abdel-Karim, A.M.; El-Shamy, A.M. "A Review on Green Corrosion Inhibitors for Protection of Archeological Metal Artifacts." *J Bio Tribo Corros.* **2022**, *8*, 35, https://doi.org/10.1007/s40735-022-00636-6.
44. Otaibi, N.A.; Hammud, H.H. Corrosion Inhibition Using Harmal Leaf Extract as an Eco-Friendly Corrosion Inhibitor. *Molecules* **2021**, *26*, 7024, https://doi.org/10.3390/molecules26227024
45. Tan, B.; Lan, W.; Zhang, S. "Passiflora edulia Sims leaves extract as renewable and degradable inhibitor for copper in sulfuric acid solution," *Coll and Sur*. **2022**, *645*, https://doi.org/10.1155/2022/3189844
46. Ijuo, G.A.; Chahul, H.F.; Eneji, I.S. Corrosion inhibition and adsorption behavior of Lonchocarpus laxiflorus extract on mild steel in hydrochloric acid. *Ew J Chem Kinet* **2016**, *1*, 21-30, https://ewemen.com/corrosion-inhibition-adsorption-behavior-lonchocarpus-laxiflorus-extract-mild-steel-hydrochloric-acid/.
47. Dahal, K. P.; Timilsena, J. N.; Gautam, M.; Bhattarai, J. Investigation on probabilistic model for corrosion failure level of buried pipelines in Kirtipur urban areas (Nepal). *J Fail Anal Prev.* **2021,** *21*, 914–926, https://doi.org/10.1007/s11668-021-01138-2.
48. Oluwatoba E.O.; Nathanael D.O.; Nureni I.; Eric B.A. and Abiodun V.E. Investigation of the corrosion inhibition potentials of some 2-(4-(substituted)arylidene)-1H-indene-1,3-dione derivatives: density functional theory and molecular dynamics simulation. Beni-Suef Univ J Basic Appl Sci 2022 11, 132 https://doi.org/10.1186/s43088-022-00313-0

49. Zeino, A.; Abdulazeez, I.; Khaled, M.; Jawish, M.W.; Obot, I.B.; Alhooshani, K. Mechanistic study of polyepoxy succinic acid (PESA) as green corrosion inhibitor on carbon steel in aerated nacl solution. *Mater. Today Commun.* **2021**, *29*, 102848, https://doi.org/10.1016/j.mtcomm.2021.102848.